INORGANIC CHEMISTRY
FRONTIERS

RESEARCH ARTICLE

View Article Online
View Journal | View Issue

Cite this: *Inorg. Chem. Front.*, 2022, **9**, 968

Highly dispersed Ru nanoclusters anchored on B,N co-doped carbon nanotubes for water splitting†

Meihong Fan,[a] Xinran Chen,[a] Mingcheng Zhang,[b] Lili Cui,[a] Xingquan He *[a] and Xiaoxin Zou *[b]

Received 31st December 2021,
Accepted 20th January 2022

DOI: 10.1039/d1qi01672e

rsc.li/frontiers-inorganic

Boron and nitrogen co-doped carbon nanotubes (CNTs)were developed as a substrate material for the loading of 2–3 nm uniform Ru clusters. Combined with a theoretical and experimental comparison, it was confirmed that B doping as well as its synergistic effect with N-doping in CNTs can effectively reduce the adsorption energy of the H intermediate at Ru site, improving the catalytic activity of the Ru cluster/CNT material for the hydrogen evolution reaction (HER) and the oxygen evolution reaction (OER). Benefiting from the synergistic effect of multi element doping and a porous tubular structure, the as-formed Ru@B, N-CNTs show excellent electrocatalytic activity for both HER and OER in alkaline conditions. An overpotential of 54 mV and 315 mV is needed to achieve a current density of 10 mA cm^{-2}, which exceeds requirements for commercial Pt/C and RuO_2. Furthermore, when assembled into an electrolyzer with Ru@B, N-CNTs as both the anode and the cathode, the cell requires a cell voltage of only 1.57 V to drive a current density of 10 mA cm^{-2} in an alkaline medium and has excellent catalytic stability for over 40 hours.

1. Introduction

Renewable energy-driven electrocatalysis to relieve the energy shortage issues that are being confronted now is appealing for the future energy transfer systems. Searching for suitable electrocatalysts is important to promote the wide application of many new energy conversion processes, including HER, OER, oxygen reduction reactions and so on.[1–5] These important electrocatalytic reactions have to rely on expensive precious metals. In order to reduce the precious metal dosage as much as possible and to improve the utilization efficiency, an effective strategy is to load precious metals onto substrate materials.[6–10] In particular, carbon-based support materials, such as graphene, carbon dots, carbon tubes, porous carbons and so on, have attracted extensive attention because of their characteristics of high specific surface area, high conductivity and corrosion resistance.[11] The abundant functional groups on the surface such as –OH, –COOH, $–NH_2$, and so on, will provide many favorable sites for the fabrication of multicomponent photo- and electroactive catalysts.[12–16] With the advances of electrocatalyst studies, it is found that the introduction of heteroatoms in a carbon support plays an important role in regulating the interaction between the support and noble metal particles, and as a result optimizes the catalytic activity. For example, N-doped CNTs have been investigated for a long time as promising substrate materials in the energy conversion and catalytic fields. The doped N atom can bond with its neighboring carbon atoms and induce a charge density rearrangement of carbon.[17–19] In particular, four N atoms in different coordination states are usually formed, that is, pyridinic-N, graphitic-N, pyrrolic-N and oxidized-N, and the former two are beneficial for the exposure of active sites.[20–23] These experimental results show the importance of rational design of heteroatoms in substrate materials.

In addition to N-doping, some new non-metallic atoms (such as B, F, P, S) have been doped into carbon to regulate the electronic structure and have gained significant research interest due to their unique electronic configuration and adjustable components.[24–27] In particular, in the latest work binary elements introduced into the carbon support at the same time show great flexibility and have good prospects for future applications. For a B, N co-doped carbon-based composite, the B–C and N–C functionalities can produce extra electronic states and modify the supported metal catalysts due to the strong metal–support interaction.[28–32] The use of bi-doping carbons acting as supports has attracted widespread research interest due to the distinct electronic structure originating from the synergistic coupling of the three atoms, B (2.04), C (2.55) and N (3.04) with different electronegativities.

[a]*School of Chemistry and Environmental Engineering, Changchun University of Science and Technology, 7089 Weixing Road, Changchun 130022, PR China. E-mail: hexingquan@hotmail.com*
[b]*State Key Laboratory of Inorganic Synthesis and Preparative Chemistry, College of Chemistry, Jilin University, 2699 Qianjin Street, Changchun 130012, China. E-mail: xxzou@jlu.edu.cn*

†Electronic supplementary information (ESI) available. See DOI: 10.1039/d1qi01672e

In addition, B or N doping can enhance the electrical conductivity of the carbon material by decreasing the band gap and making the density of states at finite and zero energy.[12,33] Joshi *et al.* reported the use of B and N co-doped reduced graphene oxide which possesses B–N, B–C, and N–C functional groups to support and stabilize the IrO_2 nanoparticles (NPs) and explored its catalytic water splitting property. However, challenges still remained due to the complexity of the system.[12] For example, although they all showed a good activity regulation effect, the understanding of surface phenomenon is very confusing and controversial. Therefore, it is very important to develop a controllable bi-doping synthetic strategy to accurately construct the doping system and establish a clear structure–activity relationship.

Herein, the effect of B and N in co-doped carbon nanotubes (B,N-CNTs) as a catalyst support for HER in alkaline medium are studied. The use of Ru nanoclusters coupled with B and N co-doped CNTs (Ru@B,N-CNTs) fabricated with a mild solution blending and post calcination method is reported. The as-obtained material can act as both efficient HER and OER catalysts that can even outperform commercial Pt/C and RuO_2 over a large current density range with outstanding stability. When further used as cathode and anode in the assembly of an overall water splitting electrolyzer in alkaline electrolyte, an applied potential of 1.57 V is needed to drive a water-splitting current density of 10 mA cm^{-2} with remarkable stability for >40 h. Comparison with B,N-CNTs, Ru@B-CNTs and Ru@B, N-CNTs as well as DFT calculations identified the synergistic effect of co-doping B and N in promoting the catalytic process.

2. Experimental section

2.1. Computation details

All the DFT calculations were carried out using the Vienna *ab initio* simulation package (VASP).[34,35] The generalized gradient approximation (GGA) was used in the form of a revised Perdew–Burke–Ernzerhof (RPBE) with Padé Approximation.[36] During all the calculation processes, the convergence threshold was set as 10^{-5} eV for energy and as 0.02 eV $Å^{-1}$ for force, and the cutoff energy of the plane-wave basis was 400 eV.[37] The Brillouin zones were sampled by Gamma centered *k*-points. All the calculations used a 3 × 3 × 1 *k*-point grid. The symmetrization was switched off and the dipolar correction was taken into consideration for all calculations.

2.2. Computations of free-energy for the hydrogen evolution reaction

A 3D carbon matrix supercell was built on a 6 × 6 × 1 unit cell for pristine carbon and the B and N atoms replaced two adjacent C atoms to give a substrate for four-Ru clusters.

The Gibbs free-energy (ΔG_{H^*}) of the adsorbed atomic hydrogen (H*) was calculated by the equation: $\Delta G_{H^*} = \Delta E_{H^*} + \Delta ZPE - T\Delta S$, where ΔE_{H^*}, ΔZPE and ΔS were the adsorption energy, zero-point energy and entropy change of H* adsorption, respectively. As proposed by Nørskov *et al.*, the ΔS was obtained using the equation: $\Delta S = S(H^*) - 1/2\ S(H_2) \approx -1/2\ S(H_2)$ and the vibrational entropy of H* was negligible, and ΔZPE was obtained using the equation: $\Delta ZPE = ZPE(H^*) - 1/2\ ZPE(H_2)$.[38] The $T\Delta S$ was calculated to be −0.205 eV because TS (H_2) was known to be 0.41 eV for H_2 at 298 K and 1 atm.

The values of all the ΔG_{H^*} and ΔE_{H^*} were obtained for different sites. Thus, the adsorption energy of atomic hydrogen was able to be calculated from eqn (1):

$$\Delta E_{H^*} = E(\text{surface} + H) - E(\text{surface}) - 1/2\ E(H_2) \quad (1)$$

where E(surface + H) and E(surface) are the energies of the surface adsorbed with one H atom, and the clear surface, respectively, and $E(H_2)$ is the energy of the hydrogen molecule in the gas phase.

2.3. Catalyst preparation

Synthesis of Ru@B,N-CNTs. $RuCl_3{\cdot}xH_2O$ (5 mg), boric acid (H_3BO_3, 20 mg) and urea (CH_4N_2O, 60 mg) were added into a beaker containing 30 mL of water and were sonicated to obtain a homogeneous solution. Carboxylated multi-walled carbon nanotubes (CNTs–COOH, 5 mg) were evenly dispersed in the mixture after sonication for another 30 min. The slurry obtained was then transferred into a 50 mL evaporating dish, heated at 80 °C for 12 h in an air-circulating. Evaporation of the slurry leaving the B,N Ru-containing precursors.

The precursors were transferred into a mortar and ground into a homogeneous fine powder, and then placed into a crucible. The sealed quartz tube was heated from room temperature to 600 °C for 2 h at a rate of 5 °C min^{-1} in a tubular furnace under Ar protection.

The experimental procedures for the synthesis of B,N-CNTs, Ru@B-CNTs and Ru@N-CNTs were almost the same as those for Ru@B,N-CNTs, except that $RuCl_3{\cdot}xH_2O$, CH_4N_2O and H_3BO_3 were not added to the starting material.

2.4. Electrochemical measurements

All the electrochemical HER and OER tests were conducted on a CHI 760e electrochemical workstation (CH Instruments) connected to a standard three-electrode cell with a carbon rod as the counter electrode, a double-salt bridge Hg/Hg_2Cl_2 electrode as the reference electrode and a catalyst-modified glassy carbon (GC) disk electrode (5 mm in diameter) as the working electrode. The working electrode was prepared by evenly loading 55 μL of 1 mg mL^{-1} catalyst ink and then sealing it with 1 μL of 0.5% Nafion. The HER and OER polarization curves were obtained using linear sweep voltammetry (LSV) at 1600 rpm in O_2 saturated 1 M KOH and N_2 saturated 1.0 M KOH solutions, respectively. All of the electrochemical tests were conducted without *iR*-correction. The scanning rate was set at 20 mV s^{-1}. The potential was normalized with respect to the reversible hydrogen electrode (RHE), according to eqn (2):

$$E_{vs.RHE} = E_{vs.Hg/Hg2Cl2} + 1.067 \quad (2)$$

A chronoamperometric test (*i*–*t*) and accelerated durability test were used to evaluate the stability of the materials, and an

impedance measurement was carried out to determine charge-transfer behavior of the materials. For comparative purposes, the catalytic activities of commercial 20 wt% Pt/C and RuO_2 with the same catalyst loading were evaluated under the same conditions as described previously.

In the overall water splitting measurement, the cathode and anode was prepared using the same procedure as the working electrode, except that nickel foam was employed as the working electrode with a working area of 0.25 cm^2.

3. Crystal and electronic structures

3.1. Preparation and characterization of the Ru@B,N-CNTs

The synthesis of the Ru@B,N-CNTs started with the ultrasonic dispersion of CNTs–COOH in the aqueous solution containing H_3BO_3, CH_4N_2O and Ru^{3+} (see Scheme 1). During this process, abundant carboxyl groups on the surface of the carbon tubes coordinated with Ru^{3+}, and the Ru^{3+} ions were uniformly anchored on the CNTs–COOH. Subsequent evaporation of water led to H_3BO_3 and CH_4N_2O covering the surface of the CNTs–COOH.[39] When the previous mixture was heat-treated in the inert atmosphere, the carboxylic acid functionalized CNTs and the coordinated Ru^{3+} on them were reduced to a graphitized CNT and Ru nanoclusters, respectively.[40] In the meantime, the H_3BO_3 and CH_4N_2O loaded on the surface of the CNTs–COOH were decomposed, and the partial B and N atoms were also incorporated into the CNTs, giving the target material, Ru@B,N-CNTs.

The X-ray diffraction (XRD) analysis was first conducted to determine the crystal phase structure of the as-prepared material (Fig. 1a). When compared with the CNTs–COOH, apart from the characteristic peaks of graphitic carbon located around 25° and 44° (labeled as a black ◆), the Ru@B,N-CNTs also showed a diffraction peak attributed to metallic Ru and weaker characteristic diffraction peaks for BN (PDF#18-0251) (labeled by a black *). According to previous reports in the literature, the formation of a B–N bond in the carbon network could improve the electron spin density, and hence, accelerate the HER and OER steps.[41] The Ru@B-CNTs and Ru@N-CNTs had nearly the same XRD patterns that were assigned to metallic Ru (Fig. S1, ESI†), indicating the successful incorporation of Ru nanoclusters into the system. The scanning electron microscopy (SEM) images of the Ru@B,N-CNTs and CNTs–COOH are shown in Fig. 1b and Fig. S2 (ESI†), and it can be seen that the Ru@B,N-CNTs have inherited the naturally curled tubular morphology structure of the starting material (CNTs–COOH) with a diameter of ≈10 nm, illustrating that the nanotube morphology of the carbon was preserved during pyrolysis. No nanoparticles can be observed after the Ru decoration, confirming the Ru NPs are ultrasmall in size.

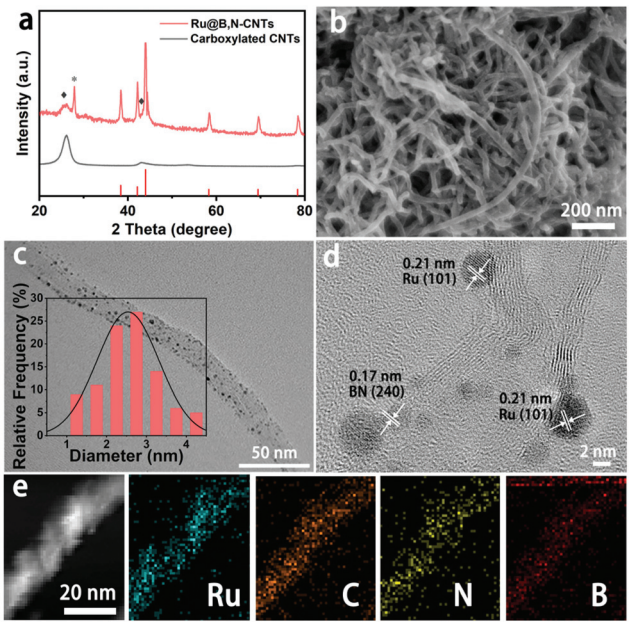

Fig. 1 (a) The XRD patterns for CNTs–COOH and Ru@B,N-CNTs. (b–d) The SEM, TEM and HRTEM images of the Ru@B,N-CNTs, the inset in (c) shows the corresponding cluster size distribution. (e) The HAADF-STEM and the corresponding element mapping images of the Ru@B,N-CNTs for B, C, N, and Ru elements.

The transmission electron microscopy (TEM) images (Fig. 1c and d) reveal that the Ru NPs are well distributed along the nanotubes with an average size of *ca.* 2.5 nm. The high-resolution TEM (HRTEM) image in Fig. 1d shows the crystalline structure of Ru and the carbon support, and the lattice fringes of graphitic carbon on the tube wall with a distance of 0.34 nm are clearly displayed. These fringes with a lattice distance of 0.21 nm were attributed to the (101) crystal plane of hexagonal Ru (PDF#06-0663). In addition, the lattice of the graphitic carbon became curved and discontinuous, indicating the generation of defects in the CNTs.[42,43] Moreover, the high angle annular dark field–scanning TEM (HAADF-STEM) image and the energy-dispersive X-ray spectroscopy (EDX) elemental mapping images of B, C, N and Ru in Fig. 1e imply that all the elements are uniformly distributed throughout CNTs.

Detailed elemental compositions and surface chemical states of the Ru@B,N-CNTs were studied by X-ray photoelectron spectroscopy (XPS). The survey spectrum in Fig. S3 (ESI†) revealed the existence of C, B, N, O and Ru on surface of the material. Peaks located at 284.6, 285.2, and 280.3 eV in Fig. 2a are assigned to the C=C bond, C–N or C–O bonds and the overlap with Ru $3d_{5/2}$, respectively.[13,44,45] The observation of the C–N species in the high-resolution C 1s spectrum indi-

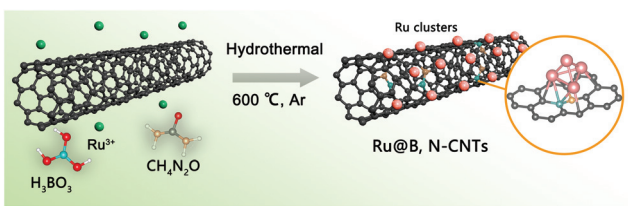

Scheme 1 Illustration of the fabrication process of the Ru@B,N-CNTs.

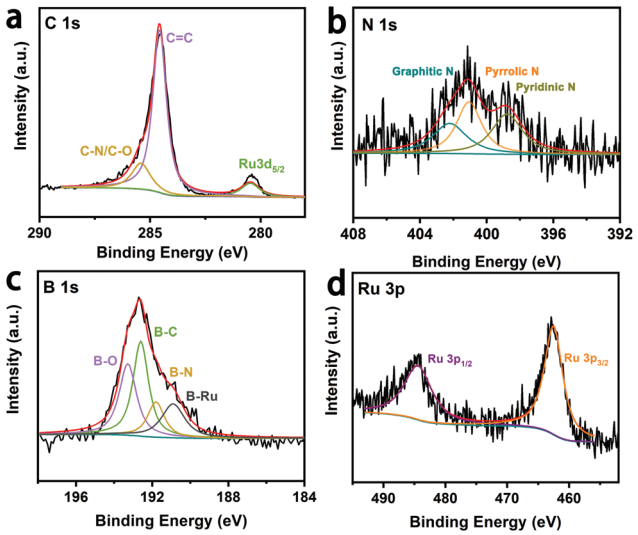

Fig. 2 High resolution XPS for (a) C 1s, (b) N 1s, (c) B 1s, and (d) Ru 3p of the Ru@B,N-CNTs.

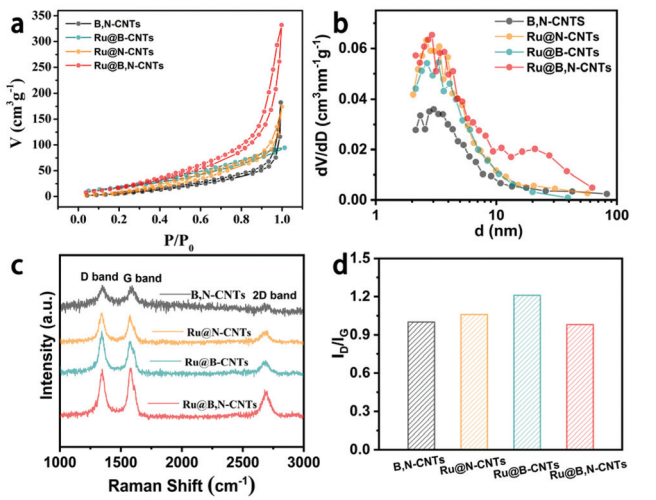

Fig. 3 (a) The N_2 sorption isotherms, (b) the corresponding pore size distributions, (c) the Raman spectra, and (d) the corresponding I_D/I_G ratios, of the B,N-CNTs, Ru@B,-CNTs, Ru@N-CNTs and Ru@B,N-CNTs.

cates that the N atoms have been incorporated in the carbon matrix. The peaks at 398.4, 399.8 and 401.6 eV (Fig. 2b) indicate the presence of pyridinic N, pyrrolic N and graphitic N. Fig. 2c shows the high-resolution B 1s XPS spectrum, and the peaks located at 190.9, 191.8, 192.6 and 193.3 eV are attributed to B–Ru bond, B–N bond, B–C bond and B–O bonds, respectively. The formation of the B–C bond further implies that the method proposed here is effective for introducing B atoms into the carbon matrix.[46] In addition, the dominant peaks of Ru $3p_{1/2}$ and Ru $3p_{3/2}$ are located at 484.4 eV and 461.9 eV, respectively, (Fig. 2d), which are the characteristic peaks attributed to nulvalent Ru.[47] This result suggests that Ru salts have been converted to metallic Ru species. Interestingly, the Ru 3p peaks of the Ru@B,N-CNTs were shifted positively by 0.74 eV when compared to the Ru@B-CNTs and Ru@N-CNTs (Fig. S4b, ESI†), whereas those peaks corresponding to B 1s in the Ru@B,N-CNTs were shifted to a less positive value relative to the B,N-CNTs (Fig. S4c, ESI†). In addition, the N 1s peaks of the Ru@B,N-CNTs were also shifted to more positive values than those of the B,N-CNTs (Fig. S4d, ESI†). These results imply that the introduction of B,N co-doping caused the transfer of electrons from Ru to the supports across their interfaces, resulting in a strong metal–support interaction between the Ru clusters and the B,N-CNT support. The synergistic interaction can give a relatively moderate hydrogen-metal binding energy on metal and improve the catalytic performance of HER.[48,49] Relative elemental amounts (at.%) on the surfaces of the four materials were investigated and the results are listed in Table S1 (ESI†). The amounts of Ru in Ru@B,N-CNTs (1.4 at%) and Ru@B-CNTs (1.4 at%) were higher than those of the Ru@N-CNTs (0.8 at%), indicating that the B doping was conducive to anchoring the Ru NPs on the CNTs.

The porous characteristics of the Ru@B,N-CNTs series samples were then investigated using the N_2 adsorption/desorption measurements. As illustrated in Fig. 3a, the four composites all show typical IV-type isotherms with a characteristic hysteresis loop at higher relative pressures, which verified the presence of mesopores. The BET surface areas of the B, N-CNTs, Ru@N-CNTs, Ru@B-CNTs, and Ru@B,N-CNTs were calculated to be 45.8, 68.5, 67.2, and 89.9 $m^2\ g^{-1}$, respectively, with almost identical pore size distributions at about 3 nm (Fig. 3b and Table S2, ESI†). The higher specific surface area of Ru@B,N-CNTs relative to those of Ru@N-CNTs and Ru@B-CNTs suggested that CH_4N_2O and H_3BO_3 not only acted as nitrogen and boron sources but were also pore forming agents in the formation of Ru decorated hetero-atom doped CNTs. This is because the organic components decomposed into gases during carbonization and induced CNT rupture, producing porous structures on the surface, which were beneficial to bubble release in the gas evolution reactions.[48,50] The abundant pores were helpful for electrolyte infiltration and mass transfer. Raman spectroscopy measurements were also carried out to study the structure of carbon in the CNTs after doping. As shown in Fig. 3c and d, the well-known D-band at 1353 cm^{-1} (disordered carbon atoms), G-band at 1590 cm^{-1} (hybridized graphitic carbon atoms) and 2D-band at 2700 cm^{-1} (graphitic sp^2-bonded carbon atoms) were observed with I_D/I_G values of 1.0, 1.06, 1.21 and 0.98 for B,N-CNTs, Ru@N-CNTs, Ru@B-CNTs and Ru@B,N-CNTs, respectively.[51] Such close intensity ratios of the Raman D to G band suggests that B or N doping and Ru loading did not affect the structure of the carbon.

3.2. Electrocatalytic hydrogen-evolving activity of the samples

The electrocatalytic properties of B,N co-doped CNTs supporting Ru clusters for HER and OER in 1 M KOH were next evaluated by employing a standard three-electrode electrochemical cell. B,N-CNTs, Ru@B-CNTs and Ru@N-CNTs were also measured under the same conditions for comparative pur-

poses. Furthermore, the 20 wt% commercial Pt/C, the benchmark noble-metal based electrocatalyst for HER and RuO_2 for OER were also included.

As shown in Fig. 4a, the B,N-CNTs showed poor catalytic activity with large overpotentials of 290 and 623 mV to reach 10 mA cm^{-2} and 100 mA cm^{-2}, respectively, for the HER. When Ru NPs were introduced into the B,N-CNTs, the as-prepared Ru/B,N-CNTs displayed distinctly improved electrocatalytic activity towards HER. It only needed overpotentials of 54 mV and 268 mV to gain current densities of 10 mA cm^{-2} and 100 mA cm^{-2} for HER, indicating the decisive role that Ru NPs played in catalyzing the HER. The overpotential of Ru@B,N-CNTs at 10 mA cm^{-2} was also significantly smaller than those of Ru@N-CNTs (111 mV) and Ru@B-CNTs (99 mV), suggesting that the doping of both B and N was beneficial for enhancing the electrocatalytic activity for the HER. The outstanding HER performance of Ru@B,N-CNTs was further confirmed by its much smaller Tafel slope (90 mV dec^{-1}) than those of Ru@B-CNTs (112 mV dec^{-1}), Ru@ N-CNTs (129 mV dec^{-1}) and B,N-CNTs (139 mV dec^{-1}) (Fig. 4b). It is worth noting that the commercial Pt/C catalyst showed a better HER activity than the Ru@B,N-CNTs at low current densities (<60 mA cm^{-2}). However, the Ru@B,N-CNTs were more active for HER than the benchmark Pt/C at high current densities (>60 mA cm^{-2}). For example, Ru@B,N-CNTs only required an overpotential of 268 mV to gain 100 mA cm^{-2}, whereas the Pt/C catalyst needed an overpotential of 313 mV to achieve the same. By considering the noble metal loadings in the catalysts, the mass activity of the Ru@B,N-CNTs material was calculated to be 1740 A g^{-1}. In fact, the Ru mass activity (j_{Ru}) of the as-obtained Ru@B,N-CNTs was among other excellent Ru-based materials (Fig. S5 and Table S6, ESI†).

The carbonization temperature had an important effect on the catalytic activity of the carbon-based materials. The Ru nanocluster loaded B,N co-doped CNTs at different carbonization temperatures, named Ru@B,N-CNTs-*T* (where *T* represents the pyrolysis temperature used to synthesize the materials), were prepared and their electrocatalytic performance for HER was also compared. It was clear from Fig. S5a and Table S3 (ESI†) that Ru@B,N-CNTs-500 and Ru@B,N-CNTs-700 needed overpotentials of 328 and 299 mV to deliver the current density of 100 mA cm^{-2}, respectively, and this was significantly larger than that of Ru@B,N-CNTs-600 (268 mV), suggesting that 600 °C was the optimal carbonization temperature.

Electrochemical impedance spectroscopy (EIS) results (Fig. S6, ESI†) indicate that theRu@B,N-CNTs had the smallest semicircle out of all the as-generated materials, that is, the smallest value of charge-transfer resistance (R_{ct}), implying that the composite structure of Ru anchored on B,N co-doped CNTs and the intimate contact between Ru and the substrate can promote charge transfer and improve the charge transfer kinetics.[52] The resistance parameters of the four materials obtained by fitting the Nyquist plots were listed in Table S4 (ESI†). The intrinsic activities of the B,N-CNTs, Ru@B-CNTs, Ru@N-CNTs, and Ru@B,N-CNTs were compared by normalizing the measured currents with respect to their electrochemical surface areas (ECSAs). A comparison of the ECSAs of the four materials and their specific activities, evaluated by the current densities produced at a fixed overpotential of 100 mV, were shown in Fig. 4c. As can be seen from the histogram, the ECSA follows the trend Ru@B,N-CNTs > Ru@B-CNTs > Ru@N-CNTs > B, N-CNTs, and their intrinsic activities for HER followed almost the same trend. With B,N co-doping into CNTs and loading of Ru clusters, two distinct phenomena follow: (1) highly dispersed

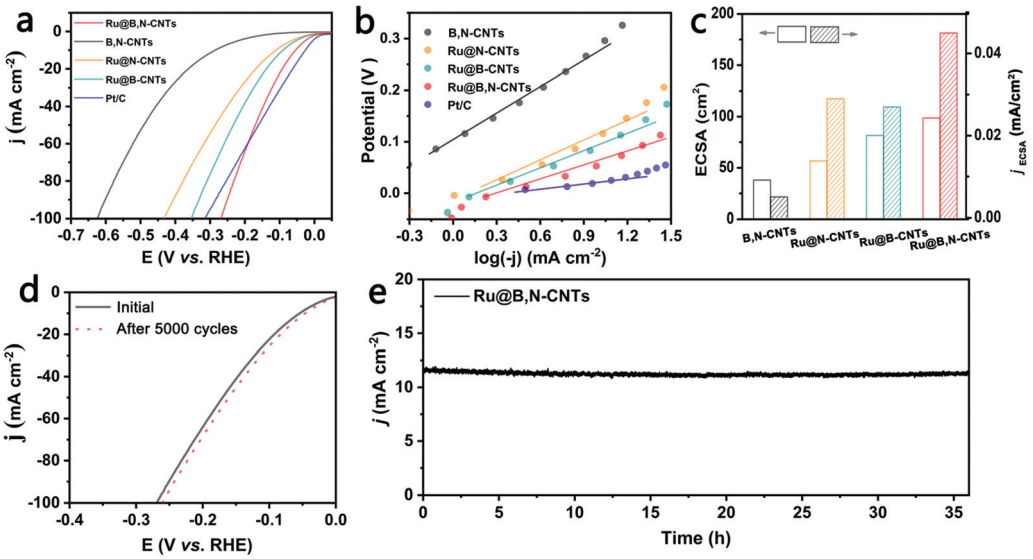

Fig. 4 (a) The linear sweep voltammetry (LSV) curves for the HER of B,N-CNTs, Ru@B-CNTs, Ru@N-CNTs, Ru@B,N-CNTs and commercial Pt/C in a 1 M KOH solution. (b) The Nyquist plots for the electrocatalysts. (c) Comparison of ECSAs and the current density produced at a fixed overpotential of 0.1 V (normalized by the ECSAs). (d) The LSV curves obtained for HER over Ru@B,N-CNTs before and after 5000 cycles of CV scans. (e) The chronoamperometric *i*–*t* curve for 36 h.

Ru NPs can fully expose the active sites; (2) the B or N doping enhances the electrical conductivity and modulates the electronic structure and adsorption capacity of the H of the carbon substrate. These two events contribute to the remarkable catalytic efficiency of the material.

Besides the high catalytic activity, the Ru@B,N-CNTs also exhibit excellent catalytic stability during electrocatalysis. The stability of the Ru@B,N-CNTs was evaluated after 5000 cycles of CV scans (Fig. 4d), which showed that the LSV curves obtained before and after the scans were almost coincident, and this indicated the durability of the material in the reaction. This was also confirmed by long-term chronoamperometric current–time (*i*–*t*) measurements, where no significant change was observed after 36 h (Fig. 4e). The previous results demonstrate overall that the Ru@B,N-CNTs is a highly active, non-Pt material, with a low noble metal consumption.

Next, the electrocatalytic performances of the as-prepared materials for OER were investigated by the LSV technique in a 1 M KOH solution saturated with O_2. As shown in Fig. 5a and Table S3 (ESI†), the OER activity of the Ru@B,N-CNTs distinctly outperforms its Ru-free analogue, Ru@B-CNTs, Ru@N-CNTs, and the commercial RuO_2 catalyst. It only needs an overpotential of 315 mV to drive a current density of 10 mA cm^{-2}, whereas the B,N-CNTs, Ru@B-CNTs, Ru@N-CNTs and the benchmark RuO_2 catalyst require overpotentials of 467, 378, 409 and 390 mV, respectively, to achieve the same. Fig. 5b shows the Tafel plots extracted from the polarization curves of the samples. A similar Tafel slope value of about 60 mV dec^{-1} was obtained, suggesting that they had the same reaction pathway, and that the water desorption to form the M–OH intermediates was the rate limiting step.[53,54] In addition, the material was also highly stable during OER, retaining its activity even after 5000 cycles of CV scans (Fig. 5c) and more than 35 h of *i*–*t* measurements (Fig. 5d).

Considering the excellent bifunctional performance of the Ru@B,N-CNTs, an overall water splitting cell using Ru@B,N-CNTs as anode and cathode was assembled. The as-fabricated electrolyzer only needed a cell voltage of 1.57 V to obtain the current density of 10 mA cm^{-2} (Fig. 6a), and it can be clearly seen in Fig. 6b that abundant bubbles were generated on both electrodes. Moreover, the electrolyzer could retain its catalytic activity at 10 mA cm^{-2} for about 40 h (Fig. 6c), indicating the outstanding stability of the Ru@B,N-CNTs as the electrocatalyst on both electrodes.

To better understand the effect of heteroatom doping on the activity enhancement of Ru-loaded boron and/or nitrogen co-doped CNTs for HER, DFT calculations were carried out using Vienna *Ab Initio* Simulation Package. As illustrated in Fig. 7a, a B,N-doped carbon layer constructed from a 6 × 6 × 1 supercell consisting of 72 atoms with one B atom and one N atom replacing adjacent carbons was used as the basic model of the CNTs, and a cluster containing four Ru atoms were decorated on the carbon layer, which had worked well in previous studies.[55] The calculation details obtained are presented in the ESI.† ΔG_{H^*}, a well-known descriptor for the theoretical prediction of catalytic activity for HER in, was calculated for Ru clusters anchored on pristine carbon, N-doped carbon (Fig. S5, ESI†) and B,N-doped carbon models. The calculation results in Fig. 7b show that ΔG_{H^*} for the three models were −0.50, −0.09 and −0.03 eV, respectively, which was consistent with the experimental results. These results imply that nitrogen and boron doping can significantly reduce ΔG_{H^*}, giving a

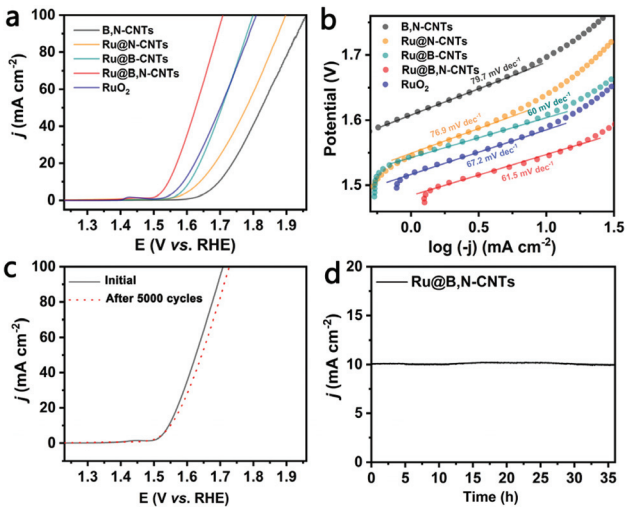

Fig. 5 (a) The linear sweep voltammetry (LSV) curves for the OER of the B,N-CNTs, Ru@B-CNTs, Ru@N-CNTs, and Ru@B,N-CNTs, and commercial RuO_2 in 1 M KOH solution. (b) The corresponding Tafel plots for the electrocatalysts. (c) The LSV curves obtained for OER over Ru@B,N-CNTs before and after 5000 cycles of CV scans. (d) The chronoamperometric *i*–*t* curve of the Ru@B,N-CNTs for 36 h.

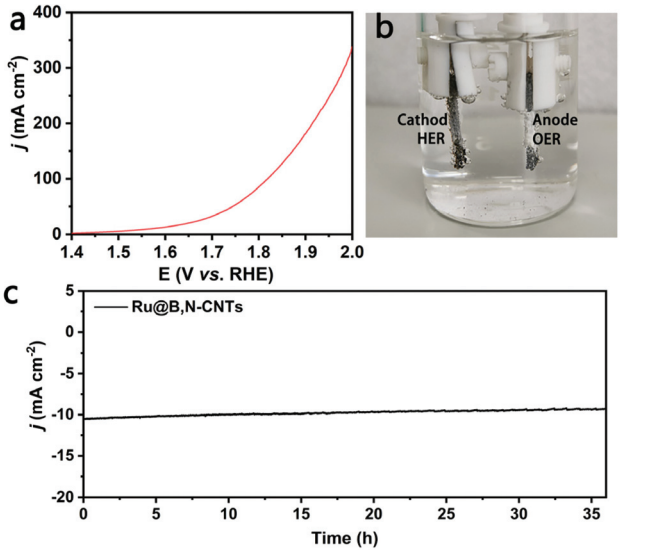

Fig. 6 (a) The LSV curve for the assembled electrolyzer in 1 M KOH employing Ru@B,N-CNT electrocatalysts as both anode and cathode. (b) A photograph of the assembled electrolyzer using Ru@B,N-CNTs as both cathode and anode. (c) The chronoamperometric *i*–*t* curve measured at an applied potential of 1.57 V for the electrolyzer assembled with Ru@B,N-CNT electrocatalysts for 36 h.

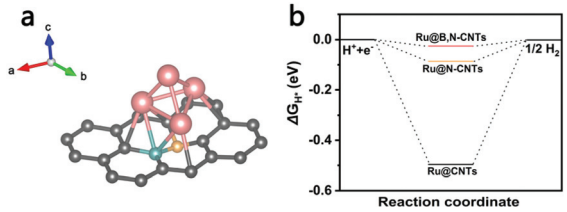

Fig. 7 (a) Optimized structures of H* adsorbed on an Ru cluster anchored on a boron and nitrogen-doped carbon layer model. The ruthenium, boron, nitrogen and carbon atoms are pink, blue, yellow and grey, respectively. (b) The HER free energy diagram. ΔG_{H^*} is calculated at the equilibrium potential of different models.

near-zero ΔG_{H^*} value at the Ru site of Ru@B,N-CNTs. Hence, Ru loaded B,N co-doped carbon nanotubes exhibit remarkable catalytic activity with the lowest ΔG_{H^*} value.

4. Conclusions

In conclusion, a B,N-co-doped carbon nanotube was designed and synthesized, as a novel substrate to support Ru nanoparticles. The as-prepared nanocomposite can efficiently catalyze both HER and OER simultaneously, and it only needs overpotentials of 54 and 315 mV to give a current density of 10 mA cm^{-2} for both HER and OER, respectively. A two-electrode cell composed of Ru@B,N-CNTs as both the anode and cathode was also assembled. The electrolyzer drives overall water splitting with a current density of 10 mA cm^{-2} at a cell voltage of 1.57 V. In addition, the DFT calculations reveal that the origin of the high electrocatalytic activity of Ru@B,N-CNTs for HER is due to the N and B doping, which synergistically modulated the electronic structure, and hence, lowered the Gibbs adsorption free energy of the Ru cluster decorated carbon nanotubes.

Conflicts of interest

There are no conflicts to declare.

Acknowledgements

This work was supported by Natural Science Foundation of Jilin Province, China (Grant No. 20210101120JC).

References

1 H. Chen, X. Liang, Y. Liu, X. Ai, T. Asefa and X. Zou, Active Site Engineering in Porous Electrocatalysts, *Adv. Mater.*, 2020, **32**, 2002435.
2 M. Jin, Y. Liu, J. Wang, X. Zhang, M. Han, Y. Zhang, G. Wang and H. Zhang, Iron covalent doping in WB2 to boost its hydrogen evolution activity, *Inorg. Chem. Front.*, 2022, DOI: 10.1039/D1QI01419F.
3 Y. Xu, T. Ren, K. Ren, S. Yu, M. Liu, Z. Wang, X. Li, L. Wang and H. Wang, Metal-organic frameworks-derived Ru-doped Co_2P/N-doped carbon composite nanosheet arrays as bifunctional electrocatalysts for hydrogen evolution and urea oxidation, *Chem. Eng. J.*, 2021, **408**, 127308.
4 R. Gao, M. Deng, Q. Yan, Z. Fang, L. Li, H. Shen and Z. Chen, Structural Variations of Metal Oxide-Based Electrocatalysts for Oxygen Evolution Reaction, *Small Methods*, 2021, **5**, 2100834.
5 H. Chen, M. Zhang, K. Zhang, Z. Li, X. Liang, X. Ai and X. Zou, Screening and Understanding Lattice Silicon-Controlled Catalytically Active Site Motifs from a Library of Transition Metal-Silicon Intermetallics, *Small*, 2022, 2107371.
6 Y. Wang, P. Zheng, M. Li, Y. Li, X. Zhang, J. Chen, X. Fang, Y. Liu, X. Yuan, X. Dai and H. Wang, Interfacial synergy between dispersed Ru sub-nanoclusters and porous NiFe layered double hydroxide on accelerated overall water splitting by intermediate modulation, *Nanoscale*, 2020, **12**, 9669–9679.
7 J. Cai, R. Javed, D. Ye, H. Zhao and J. Zhang, Recent progress in noble metal nanocluster and single atom electrocatalysts for the hydrogen evolution reaction, *J. Mater. Chem. A*, 2020, **8**, 22467–22487.
8 T. Gao, X. Li, X. Chen, C. Zhou, Q. Yue, H. Yuan and D. Xiao, Ultra-fast preparing carbon nanotube-supported trimetallic Ni, Ru, Fe heterostructures as robust bifunctional electrocatalysts for overall water splitting, *Chem. Eng. J.*, 2021, **424**, 130416.
9 X. Mu, X. Gu, R. Zhou, L. Li, G. Lu, C. Chen, S. Liu, S. Mu and W. Chen, Metastable five-fold twinned Ru incorporated Cu nanosheets with Pt-like hydrogen evolution kinetics, *Chem. Eng. J.*, 2022, **428**, 131099.
10 S.-Y. Bae, J. Mahmood, I.-Y. Jeon and J.-B. Baek, Recent advances in ruthenium-based electrocatalysts for the hydrogen evolution reaction, *Nanoscale Horiz.*, 2020, **5**, 43–56.
11 Y. Sun, Y. Zhou, Y. Liu, Q. Wu, M. Zhu, H. Huang, Y. Liu, M. Shao and Z. Kang, A photoactive process cascaded electrocatalysis for enhanced methanol oxidation over Pt-MXene-TiO_2 composite, *Nano Res.*, 2020, **13**, 2683–2690.
12 P. Joshi, R. Yadav, M. Hara, T. Inoue, Y. Motoyama and M. Yoshimura, Contribution of B,N-co-doped reduced graphene oxide as a catalyst support to the activity of iridium oxide for oxygen evolution reaction, *J. Mater. Chem. A*, 2021, **9**, 9066–9080.
13 Q. Xie, Z. Wang, L. Lin, Y. Shu, J. Zhang, C. Li, Y. Shen and H. Uyama, Nanoscaled and Atomic Ruthenium Electrocatalysts Confined Inside Super-Hydrophilic Carbon Nanofibers for Efficient Hydrogen Evolution Reaction, *Small*, 2021, **17**, 2102160.
14 J. Luo, L. Yang, T. Li, L. Yang, X. Luo and J. C. Crittenden, Three-dimensional electrode interface assembled from rGO nanosheets and carbon nanotubes for highly electro-

catalytic oxygen reduction, *Chem. Eng. J.*, 2019, **378**, 122127.
15 H. Yu, L. Hui, Y. Xue, Y. Liu, Y. Fang, C. Xing, C. Zhang, D. Zhang, X. Chen, Y. Du, Z. Wang, Y. Gao, B. Huang and Y. Li, 2D graphdiyne loading ruthenium atoms for high efficiency water splitting, *Nano Energy*, 2020, **72**, 104667.
16 H. Wang, J. Cao, Y. Zhou, X. Wang, H. Huang, Y. Liu, M. Shao and Z. Kang, Carbon dots modified Ti_3C_2Tx-based fibrous supercapacitor with photo-enhanced capacitance, *Nano Res.*, 2021, **14**, 3886–3892.
17 Y. Huang, Y. Li, Q. Luo and X. Huang, One-step preparation of functional groups-rich graphene oxide and carbon nanotubes nanocomposite for efficient magnetic solid phase extraction of glucocorticoids in environmental waters, *Chem. Eng. J.*, 2021, **406**, 126785.
18 S. H. Yang, S.-K. Park and Y. C. Kang, Mesoporous $CoSe_2$ nanoclusters threaded with nitrogen-doped carbon nanotubes for high-performance sodium-ion battery anodes, *Chem. Eng. J.*, 2019, **370**, 1008–1018.
19 Y. J. Oh, J. H. Kim and Y. C. Kang, Yolk–shell-structured manganese oxide/nitride composite powders comprising cobalt-nanoparticle-embedded nitrogen-doped carbon nanotubes as cathode catalysts for long-life-cycle lithium–oxygen batteries, *Chem. Eng. J.*, 2019, **373**, 86–94.
20 Z. Peng, Y. Yu, D. Jiang, Y. Wu, B. Y. Xia and Z. Dong, N-doped carbon shell coated CoP nanocrystals encapsulated in porous N-doped carbon substrate as efficient electrocatalyst of water splitting, *Carbon*, 2019, **144**, 464–471.
21 D. Yu, Q. Zhang and L. Dai, Highly Efficient Metal-Free Growth of Nitrogen-Doped Single-Walled Carbon Nanotubes on Plasma-Etched Substrates for Oxygen Reduction, *J. Am. Chem. Soc.*, 2010, **132**, 15127–15129.
22 M. Yuan, S. Zhang, L. Lin, Z. Sun, H. Yang, H. Li, G. Sun, C. Nan and S. Ma, Manganese Carbodiimide Nanoparticles Modified with N-Doping Carbon: A Bifunctional Cathode Electrocatalyst for Aprotic Li–O2 Battery, *ACS Sustainable Chem. Eng.*, 2019, **7**, 17464–17473.
23 S. Chen, J. Duan, M. Jaroniec and S.-Z. Qiao, Nitrogen and Oxygen Dual-Doped Carbon Hydrogel Film as a Substrate-Free Electrode for Highly Efficient Oxygen Evolution Reaction, *Adv. Mater.*, 2014, **26**, 2925–2930.
24 H. Zhang, T. Wang, A. Sumboja, W. Zang, J. Xie, D. Gao, S. J. Pennycook, Z. Liu, C. Guan and J. Wang, Integrated Hierarchical Carbon Flake Arrays with Hollow P-Doped $CoSe_2$ Nanoclusters as an Advanced Bifunctional Catalyst for Zn–Air Batteries, *Adv. Funct. Mater.*, 2018, **28**, 1804846.
25 X. Wang, M. Hou, Z. Shi, X. Liu, I. Mizota, H. Lou, B. Wang and X. Hou, Regulate Phosphorus Configuration in High P-Doped Hard Carbon as a Superanode for Sodium Storage, *ACS Appl. Mater. Interfaces*, 2021, **13**, 12059–12068.
26 P. Li, M. Wang, S. Huang and Y. Su, Phosphorus- and fluorine-co-doped carbon nitride: modulated visible light absorption, charge carrier kinetics and boosted photocatalytic hydrogen evolution, *Dalton Trans.*, 2021, **50**, 14110–14114.
27 L. Lin, N. Miao, G. G. Wallace, J. Chen and D. A. Allwood, Engineering Carbon Materials for Electrochemical Oxygen Reduction Reactions, *Adv. Energy Mater.*, 2021, **11**, 2100695.
28 H. Tabassum, R. Zou, A. Mahmood, Z. Liang and S. Guo, A catalyst-free synthesis of B, N co-doped graphene nanostructures with tunable dimensions as highly efficient metal free dual electrocatalysts, *J. Mater. Chem. A*, 2016, **4**, 16469–16475.
29 L. Han, H. Huang, J. Li, Z. Yang, X. Zhang, D. Zhang, X. Liu, M. Xu and L. Pan, Novel zinc–iodine hybrid supercapacitors with a redox iodide ion electrolyte and B, N dual-doped carbon electrode exhibit boosted energy density, *J. Mater. Chem. A*, 2019, **7**, 24400–24407.
30 N. Fu, Y. Liu, R. Liu, X. Wang and Z. Yang, Metal Cation-Assisted Synthesis of Amorphous B, N Co-Doped Carbon Nanotubes for Superior Sodium Storage, *Small*, 2020, **16**, 2001607.
31 Y. Chang, C. Yuan, Y. Li, C. Liu, T. Wu, B. Zeng, Y. Xu and L. Dai, Controllable fabrication of a N and B co-doped carbon shell on the surface of TiO_2 as a support for boosting the electrochemical performances, *J. Mater. Chem. A*, 2017, **5**, 1672–1678.
32 V. Ramalingam, P. Varadhan, H.-C. Fu, H. Kim, D. Zhang, S. Chen, L. Song, D. Ma, Y. Wang, H. N. Alshareef and J.-H. He, Heteroatom-Mediated Interactions between Ruthenium Single Atoms and an MXene Support for Efficient Hydrogen Evolution, *Adv. Mater.*, 2019, **31**, 1903841.
33 S. Wang, E. Iyyamperumal, A. Roy, Y. Xue, D. Yu and L. Dai, Vertically Aligned BCN Nanotubes as Efficient Metal-Free Electrocatalysts for the Oxygen Reduction Reaction: A Synergetic Effect by Co-Doping with Boron and Nitrogen, *Angew. Chem., Int. Ed.*, 2011, **50**, 11756–11760.
34 G. Kresse and J. Furthmüller, Efficiency of *ab initio* total energy calculations for metals and semiconductors using a plane-wave basis set, *Comput. Mater. Sci.*, 1996, **6**, 15–50.
35 G. Kresse and J. Furthmüller, Efficient iterative schemes for ab initio total-energy calculations using a plane-wave basis set, *Phys. Rev. B: Condens. Matter Mater. Phys.*, 1996, **54**, 11169–11186.
36 M. Hammouchi, E. H. El Boudouti, A. Nougaoui, B. Djafari-Rouhani, M. L. H. Lahlaouti, A. Akjouj and L. Dobrzynski, Acoustic waves in finite superlattices: Influence of buffer layers, *Phys. Rev. B: Condens. Matter Mater. Phys.*, 1999, **59**, 1999–2010.
37 P. E. Blöchl, Projector augmented-wave method, *Phys. Rev. B: Condens. Matter Mater. Phys.*, 1994, **50**, 17953–17979.
38 J. K. Nørskov, T. Bligaard, A. Logadottir, J. R. Kitchin, J. G. Chen, S. Pandelov and U. Stimming, Trends in the Exchange Current for Hydrogen Evolution, *J. Electrochem. Soc.*, 2005, **152**, J23.
39 C. Wang, X. Zhang, J. Wang, Y. Ma, S. Lv, J. Xiang, M. Chu, T. Sun and C. Qin, Boron/Nitrogen/Oxygen Co-Doped Carbon with High Volumetric Performance for Aqueous Symmetric Supercapacitors, *J. Electrochem. Soc.*, 2018, **165**, A856–A866.

40 X. Xiao, X. Wang, X. Jiang, S. Song, D. Huang, L. Yu, Y. Zhang, S. Chen, M. Wang, Y. Shen and Z. Ren, In Situ Growth of Ru Nanoparticles on (Fe,Ni)(OH)2 to Boost Hydrogen Evolution Activity at High Current Density in Alkaline Media, *Small Methods*, 2020, **4**, 1900796.
41 W. K. Hsu, S. Firth, P. Redlich, M. Terrones, H. Terrones, Y. Q. Zhu, N. Grobert, A. Schilder, R. J. H. Clark, H. W. Kroto and D. R. M. Walton, Boron-doping effects in carbon nanotubes, *J. Mater. Chem.*, 2000, **10**, 1425–1429.
42 F. Yang, X. Chen, Z. Li, D. Wang, L. Liu and J. Ye, Ultrathin FeP Nanosheets as an Efficient Catalyst for Electrocatalytic Water Oxidation: Promoted Intermediates Adsorption by Surface Defects, *ACS Appl. Energy Mater.*, 2020, **3**, 3577–3585.
43 H. Guo, C.-G. Niu, C.-Y. Feng, C. Liang, L. Zhang, X.-J. Wen, Y. Yang, H.-Y. Liu, L. Li and L.-S. Lin, Steering exciton dissociation and charge migration in green synthetic oxygen-substituted ultrathin porous graphitic carbon nitride for boosted photocatalytic reactive oxygen species generation, *Chem. Eng. J.*, 2020, **385**, 123919.
44 E. Desimoni and B. Brunetti, X-Ray Photoelectron Spectroscopic Characterization of Chemically Modified Electrodes Used as Chemical Sensors and Biosensors: A Review, *Chemosensors*, 2015, **3**, 337–343.
45 H. Chen, X. Huang, L.-J. Zhou, G.-D. Li, M. Fan and X. Zou, Electrospinning Synthesis of Bimetallic Nickel–Iron Oxide/Carbon Composite Nanofibers for Efficient Water Oxidation Electrocatalysis, *ChemCatChem*, 2016, **8**, 992–1000.
46 Y. Qiao, P. Yuan, C.-W. Pao, Y. Cheng, Z. Pu, Q. Xu, S. Mu and J. Zhang, Boron-rich environment boosting ruthenium boride on B, N doped carbon outperforms platinum for hydrogen evolution reaction in a universal pH range, *Nano Energy*, 2020, **75**, 104881.
47 M. Zhao, H. Li, W. Li, J. Li, L. Yi, W. Hu and C. M. Li, Ru-Doping Enhanced Electrocatalysis of Metal–Organic Framework Nanosheets toward Overall Water Splitting, *Chem. – Eur. J.*, 2020, **26**, 17091–17096.
48 M. Li, H. Wang, W. Zhu, W. Li, C. Wang and X. Lu, RuNi Nanoparticles Embedded in N-Doped Carbon Nanofibers as a Robust Bifunctional Catalyst for Efficient Overall Water Splitting, *Adv. Sci.*, 2020, **7**, 1901833.
49 Q. Yao, B. Huang, N. Zhang, M. Sun, Q. Shao and X. Huang, Channel-Rich RuCu Nanosheets for pH-Universal Overall Water Splitting Electrocatalysis, *Angew. Chem., Int. Ed.*, 2019, **58**, 13983–13988.
50 S. Zhang, L. Xu, J. Wu, Y. Yang, C. Zhang, H. Tao, J. Lin, L. Huang, W. Fang, K. Shi and X. Dong, Femtosecond laser micro-nano processing for boosting bubble releasing of gas evolution reactions, *Nano Res.*, 2022, **15**, 1672–1679.
51 D. J. Late, U. Maitra, L. S. Panchakarla, U. V. Waghmare and C. N. R. Rao, Temperature effects on the Raman spectra of graphenes: dependence on the number of layers and doping, *J. Phys.: Condens. Matter*, 2011, **23**, 055303.
52 Y.-L. Wu, X. Li, Y.-S. Wei, Z. Fu, W. Wei, X.-T. Wu, Q.-L. Zhu and Q. Xu, Ordered Macroporous Superstructure of Nitrogen-Doped Nanoporous Carbon Implanted with Ultrafine Ru Nanoclusters for Efficient pH-Universal Hydrogen Evolution Reaction, *Adv. Mater.*, 2021, **33**, 2006965.
53 J. Li, Y. Liu, H. Chen, Z. Zhang and X. Zou, Design of a Multilayered Oxygen-Evolution Electrode with High Catalytic Activity and Corrosion Resistance for Saline Water Splitting, *Adv. Funct. Mater.*, 2021, **31**, 2101820.
54 Z. Liu, H. Liu, X. Gu and L. Feng, Oxygen evolution reaction efficiently catalyzed by a quasi-single-crystalline cobalt fluoride, *Chem. Eng. J.*, 2020, **397**, 125500.
55 W. Li, Y. Liu, M. Wu, X. Feng, S. A. T. Redfern, Y. Shang, X. Yong, T. Feng, K. Wu, Z. Liu, B. Li, Z. Chen, J. S. Tse, S. Lu and B. Yang, Carbon-Quantum-Dots-Loaded Ruthenium Nanoparticles as an Efficient Electrocatalyst for Hydrogen Production in Alkaline Media, *Adv. Mater.*, 2018, **30**, 1800676.

